PHYSICAL REVIEW B **88**, 081108(R) (2013)

Termination-dependent topological surface states of the natural superlattice phase Bi_4Se_3

Q. D. Gibson,[1] L. M. Schoop,[1] A. P. Weber,[2,3] Huiwen Ji,[1] S. Nadj-Perge,[4] I. K. Drozdov,[4] H. Beidenkopf,[4] J. T. Sadowski,[5] A. Fedorov,[6] A. Yazdani,[4] T. Valla,[7] and R. J. Cava[1,*]

[1]*Department of Chemistry, Princeton University, Princeton, New Jersey 08544, USA*
[2]*National Synchrotron Light Source, Brookhaven National Lab, Upton, New York 11973, USA*
[3]*Department of Physics and Astronomy, University of Missouri-Kansas City, Kansas City, Missouri 64110, USA*
[4]*Department of Physics, Princeton University, Princeton, New Jersey 08544, USA*
[5]*Center for Functional Nanomaterials, Brookhaven National Lab, Upton, New York 11973, USA*
[6]*Advanced Light Source, Lawrence Berkeley National Laboratory, Berkeley, California 94720, USA*
[7]*Condensed Matter Physics and Materials Science Department, Brookhaven National Lab, Upton, New York 19973, USA*

(Received 18 April 2013; published 30 August 2013)

We describe the topological surface states of Bi_4Se_3, a compound in the infinitely adaptive Bi_2-Bi_2Se_3 natural superlattice phase series, determined by a combination of experimental and theoretical methods. Two observable cleavage surfaces, terminating at Bi or Se, are characterized by angle-resolved photoelectron spectroscopy and scanning tunneling microscopy, and modeled by *ab initio* density functional theory calculations. Topological surface states are observed on both surfaces, but with markedly different dispersions and Kramers point energies. Bi_4Se_3 therefore represents the only known compound with different topological states on differently terminated, easily distinguished and stable surfaces.

DOI: 10.1103/PhysRevB.88.081108 PACS number(s): 71.20.−b, 79.60.Bm, 73.20.−r, 71.70.Ej

Three-dimensional topological insulators (3D TIs) are a new class of materials that exhibit topologically protected helical metallic topological surface states (TSS) and a bulk band gap.[1–12] The great interest in 3D TIs is partly due to the fact that they necessarily host exotic bound states at their boundaries when interfaced with other nontopological or topological materials.[13] In addition, several theoretical studies have predicted that novel properties may emerge when topological insulators are interlaced with other materials in a regular superlattice.[14,15] In order to pursue these promising avenues, however, various experimental challenges have to be solved. For example, a basic understanding of the surface band structures of more complex topological materials, while highly desirable, is not trivial. Although there have been studies of different materials at the interface of 3D TIs,[16,17] and on different surface terminations of the same material,[18,19] no in-depth study of the TSS and electronic band structure of a complex topological material or a true bulk topological superlattice material has yet been reported.

Here, we investigate the properties of Bi_4Se_3, the simplest topological superlattice material, consisting of single Bi_2 layers interleaved with single Bi_2Se_3 layers in a 1:1 ratio[20] [Fig. 1(a)]. While bulk Bi_2Se_3 is a model 3D TI, an isolated Bi_2 layer is predicted to be a 2D TI;[21] combining these two building blocks into a 3D superlattice offers a unique possibility for studying the effects of interlayer interactions. We investigate the electronic structure of this material experimentally via angle-resolved photoemission spectroscopy (ARPES) and scanning tunneling microscopy (STM) and theoretically via *ab initio* density functional theory (DFT) calculations. We observe two types of surfaces after cleaving the crystal, corresponding to Bi_2- and Bi_2Se_3-terminated terraces. We find that both terminations exhibit TSS, but with substantially different Kramers point energies and dispersions. We show that many features of the surface band structure can be derived from the idealized case of weakly coupled Bi_2 and Bi_2Se_3 layers where the interaction between these building blocks is responsible for the different TSSs. Bi_4Se_3 and related $(Bi_2)_m(Bi_2Se_3)_n$ (Ref. 22) superlattice phases provide a unique opportunity for studying the coexistence of multiple types of topological surface states on distinct, stable, and separable cleavage surfaces in the same material.

Crystals of Bi_4Se_3 were grown by slow cooling a Bi-rich melt. The crystal structure and quality were confirmed by x-ray diffraction. The ARPES experiments were carried out on a Scienta SES-100 electron spectrometer at beamline 12.0.1 of the Advanced Light Source. The spectra were recorded at photon energies ranging from 35 to 100 eV, with a combined instrumental energy resolution of ∼15 meV and an angular resolution better than ±0.07°. The combined spatial resolution, dependent upon precise linear motion control of the sample and the 60-μm photoemission spot size of the beam, was better than 80 μm. Samples were cleaved at 15–20 K under ultrahigh vacuum (UHV) conditions. The temperature was measured using a silicon sensor mounted near the sample. Photoemission electron microscopy (PEEM) experiments were carried out at the XPEEM/LEEM end station at the National Synchrotron Light Source beamline U5UA at room temperature with 47.8 eV photons using an Elmitec SPELEEM III microscope. All the samples were cut from the same bulk piece and cleaved and measured in ultrahigh vacuum conditions (base pressure better than 2×10^{-9} Pa in the ARPES chamber and better than 2×10^{-8} Pa in the PEEM chamber). Samples for STM measurements were cleaved *in situ* at room temperature under ultrahigh vacuum conditions, with the measurements performed at 4.2 K. Both Bi_2 and Bi_2Se_3 surfaces are exposed in the cleaves; there is no known dependence of terrace size on cleavage temperature.

Surface electronic-structure calculations were performed in the framework of density functional theory using the WIEN2K code[23] with a full-potential linearized augmented

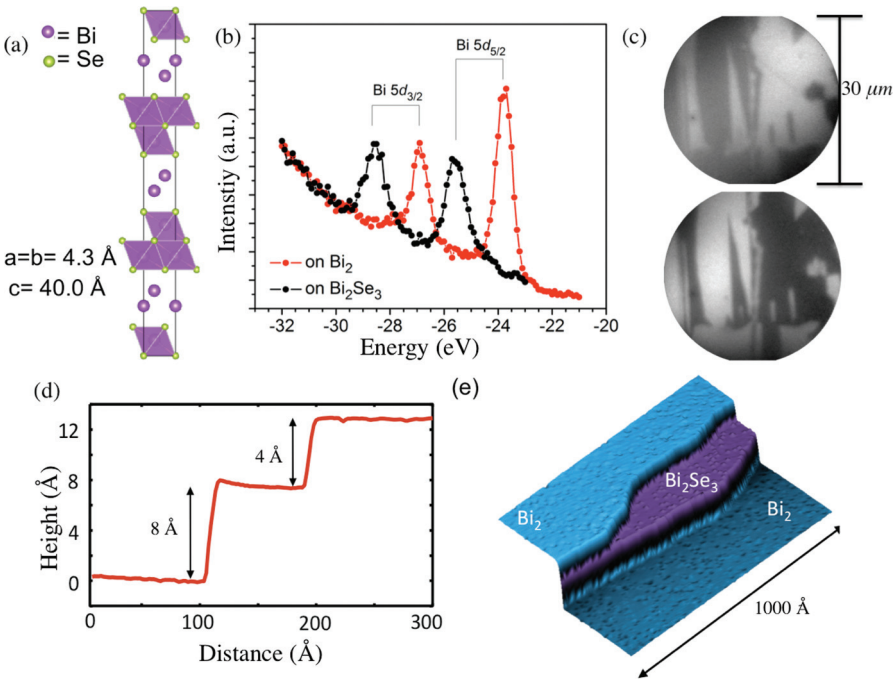

FIG. 1. (Color online) (a) Unit cell of Bi_4Se_3 projected down the a axis. Bi-Se polyhedra are shaded to highlight the alternating quintuple layer-bilayer structure. (b) Micro-XPS spectra for the Bi 5d core level, taken from Bi_2 and Bi_2Se_3 regions, respectively; spot size 2 micrometers. (c) PEEM images obtained using respective Bi 5d $\frac{5}{2}$ core levels showing high intensity (bright) for the Se termination (top) and for the Bi termination (bottom). The field of view is 30 micrometers. The average domain size of the different terminations is approximately equivalent. (d) STM linecut across a step edge showing the heights of the Bi_2 and Bi_2Se_3 steps (4 and 8 Å, respectively). (e) False color STM topography image close to the step edge from (d) where both types of surfaces can be identified.

plane-wave and local orbitals basis together with the Perdew-Burke-Ernzerhof parametrization of the generalized gradient approximation,[24] using a slab geometry. The plane-wave cutoff parameter $R_{MT}K_{\max}$ was set to 7 and the Brilloun zone (BZ) was sampled by 9 k points, or 100 k points in the case of the weakly coupled Bi_2 and Bi_2Se_3 layers. Spin-orbit coupling (SOC) was included. For the Bi_2-terminated surface, a slab was constructed of 5 Bi_2Se_3 layers and 6 Bi_2 layers, with 10 Å of vacuum between adjacent slabs. For the Bi_2Se_3-terminated surface, a slab was constructed of 6 Bi_2Se_3 layers and 5 Bi_2 layers. To calculate weakly coupled Bi_2 and Bi_2Se_3 layers, a rhombohedral unit cell was used that retains all of the parameters of Bi_4Se_3 but with an artificial interlayer distance of 5 Å. The experimentally determined lattice parameters and atom positions were used to construct the slabs. The contribution of the surface atoms to the overall surface electronic structure was determined by calculating the partial contribution of each atomic basis set to the wave functions at all k points.

Bi- and Se-rich regions on cleaved surfaces, corresponding to Bi_2 bilayers and Bi_2Se_3 quintuple layers, were identified in PEEM by difference in work function (not shown). Subsequently, microspot x-ray photoemission spectra (micro-XPS) for the Bi 5d core level [Fig. 1(b)] were obtained from Bi_2 and Bi_2Se_3 regions, respectively. The spectra taken on the Bi_2Se_3 are shifted by about 1.8 eV towards higher binding energies for both components of the Bi 5d doublet. We further utilized the respective Bi 5d $\frac{5}{2}$ component from both regions to obtain PEEM images of the surface [Fig. 1(c)]. The terraces with different terminations are clearly visible, ranging in size from a few μm^2 to $\sim(100\ \mu m)^2$. The fine features in the topography measured in STM clearly reveal two types of surfaces [Figs. 1(d) and 1(e)]. The topography of the region close to the step edge allows us to identify the surfaces; the measured step heights are approximately 4 and 8 Å, consistent with the first and the second surfaces being a Bi_2 bilayer and Bi_2Se_3 quintuple layers, respectively. Domains suitable for quasiparticle interference (QPI) measurements were observed.

While the 60-μm ARPES spot size is comparable to the domain size of the different terminations, and thus insufficient to completely resolve the two terminations, Bi- and Se-predominated surface terminations are easily distinguished, allowing for the clear determination of the surface electronic structures of both terminations. Figure 2(a) shows the ARPES spectra of the Se- and Bi-rich surfaces, reflecting significant differences between the two terminations. The Bi 5d and Se 3d core levels in Fig. 2(b) were measured at exactly the same locations where the ARPES spectra from Fig. 2(a) were recorded, enabling the identification of two different surface states with two terminations.

Contrary to expectations, the Bi_2 termination exhibits nearly linear Dirac surface states similar to those observed in topological insulators such as Bi_2Se_3, although with the holelike dispersion, while the Bi_2Se_3 termination exhibits a nonlinearly dispersing surface state. The existence of these surface states is consistent with the band inversion at Γ for bulk Bi_4Se_3 (indicating a nontrival $Z2$ invariant) and with the TSS observed earlier on $Bi_4Se_{2.4}S_{0.6}$.[25]

The calculation for the Bi_2Se_3 termination [left, Fig. 2(c)] shows the same type of nonlinear surface state that is experimentally observed by ARPES. The calculated electronic structure indicates that the surface state is nontrivial; there is a symmetry-allowed crossing at about -0.5 eV at $\bar{\Gamma}$ and the state crosses the continuous gap in the bulk bands an odd number of times along $\bar{\Gamma}$-$\bar{M}$, therefore satisfying the odd-crossing criterion for a topological surface state. The state is similar to the states seen on the surface of topological elemental Sb.[26]

The calculated surface states for the Bi_2 termination [right, Fig. 2(c)] clearly show a surface Dirac cone. A close look reveals that the surface contribution vanishes precipitously upon joining the semimetallic bulk bands slightly above E_F, meaning that the surface state crossing the continuous

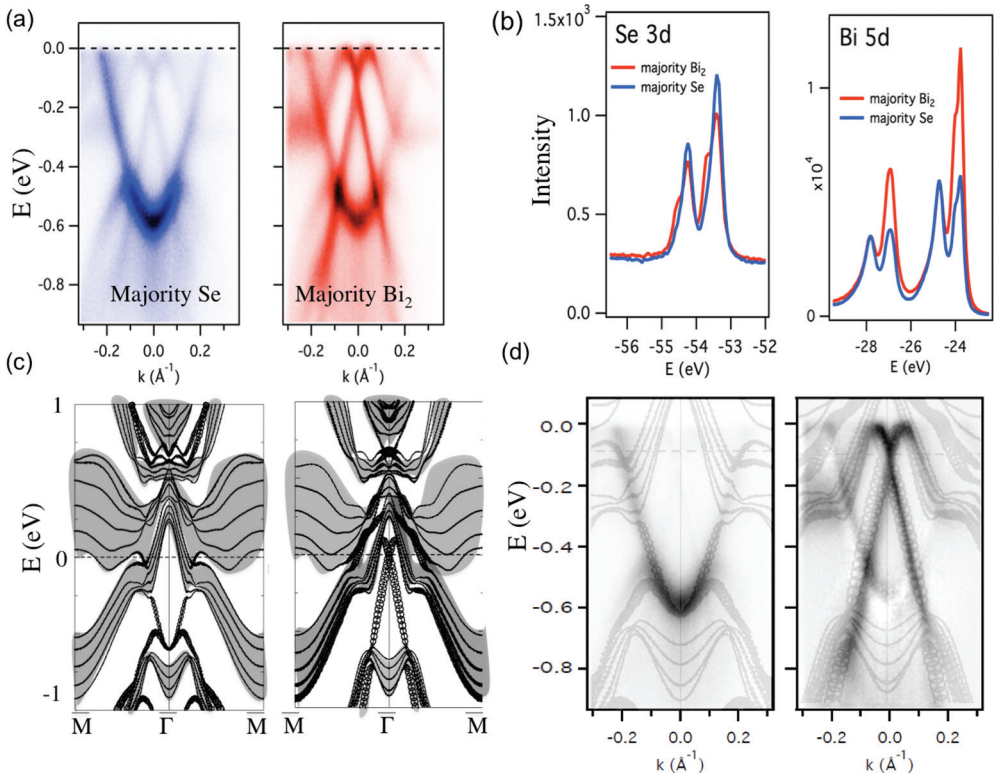

FIG. 2. (Color online) (a) Raw ARPES data for cleavage surfaces dominated by Se termination (left) and Bi termination (right). (b) Photoemission spectra of Se 3*d* and Bi 3*d* levels used to identify Bi_2Se_3- and Bi_2-rich regions. (c) Calculated surface electronic structure for the Bi_2Se_3-terminated (left) and Bi_2-terminated (right) surfaces of Bi_4Se_3. Bulk bands are shaded. (d) Calculated surface electronic structures of Bi_2Se_3- (left) and Bi_2- (right) terminated surfaces, overlaid on the surface states observed experimentally by ARPES, on the same scale.

gap an odd number of times along $\bar{\Gamma} - \bar{M}$. The observed surface electronic structure bears resemblance to that found on single Bi_2 layers deposited on Bi_2Te_3, which has been suggested as a platform for quantum spin Hall (QSH) edge states.[17] Comparisons of the observed and calculated surface electronic structures of the Bi_2- and Bi_2Se_3-terminated surfaces of Bi_4Se_3 are shown in Fig. 2(d), with the calculations overlaid on the experimental data, displaying a good match between calculation and experiment. The real crystal is slightly *n* doped (by about 0.1 eV) when compared to the calculations.

To explain the overall surface-state electronic structure of Bi_4Se_3, the calculated electronic structure was compared to that of weakly coupled Bi_2 and Bi_2Se_3 layers (separated by 5 Å) [Fig. 3(a)]. The weak coupling was confirmed by a lack of dispersion along k_z. In the weak-coupling case, there is a distinct band inversion between the conduction band ($CB1_{Bi_2Se_3}$) of Bi_2Se_3 and the valence bands ($VB1_{Bi_2}$ and $VB2_{Bi_2}$) of Bi_2, with a small SOC induced gap (less than 20 meV) appearing between $VB1_{Bi_2}$ and $CB1_{Bi_2Se_3}$ around E_F along Γ-F and Γ-L. This is a topological band inversion; the parity of the $VB1_{Bi_2}$ is opposite that of both $CB1_{Bi_2Se_3}$ and $VB2_{Bi_2}$. There is also an avoided crossing gap (about 200 meV) between $VB2_{Bi_2}$ and $CB1_{Bi_2Se_3}$. The Kramers point energies and dispersions of the Bi_2- and Bi_2Se_3-terminated TSS correspond extremely closely to the $VB2_{Bi_2}$ maximum and $CB1_{Bi_2Se_3}$ minimum, respectively, of the weakly coupled case. This suggests that the Kramers point energies of the TSS are determined by energy levels intrinsic to the individual, isolated version of the layer that hosts them. This idealized weakly coupled case would be a weak topological semimetal, with a parity inversion at both Γ and Z points. As interlayer bonding

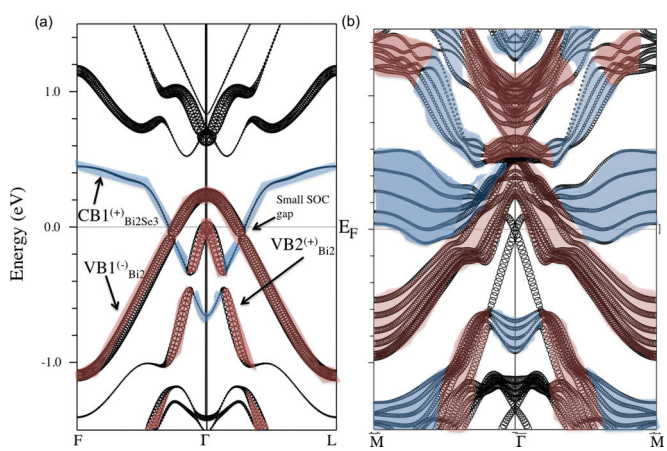

FIG. 3. (Color online) (a) The calculated electronic structure of weakly coupled Bi_2 and Bi_2Se_3 layers. Both F and L would project to $\bar{M}$ in the surface electronic structure. The parities of the relevant bands are noted in the superscript. The Bi_2-based valence bands and the Bi_2Se_3-based conduction band are shaded in red and blue, respectively. (b) The calculated surface-state electronic structure for the Bi_2-terminated surface of Bi_4Se_3, shown for comparison to the idealized case. Heavier plotting shows the contribution of the Bi_2 layers. Bulk bands derived mainly from Bi_2 and Bi_2Se_3 are shaded red and blue, respectively. For both (a) and (b), circle size is proportional to the amount of Bi_2 bilayer character.

is negligible in this case, the band inversion is driven by charge transfer from the Bi_2 layer to the more electronegative Bi_2Se_3 layer, hence the overlap of the valence bands of Bi_2 and the conduction band of Bi_2Se_3.

Figure 3(b) shows the corresponding Bi_2-derived features in the more realistic surface band structure that includes the full interlayer coupling. Full coupling between the layers moves $CB1_{Bi_2Se_3}$ up in energy and the valence bands of Bi_2 down, retaining the band inversion at Γ but uninverting the bands at Z in the bulk electronic structure, allowing for the nontrivial $Z2$ invariant due to parity inversion at Γ in the bulk electronic structure reported earlier.[25] Full coupling also increases the avoided crossing gap between $CB1_{Bi_2Se_3}$ and $VB2_{Bi_2}$ to about 0.6 eV, leaving $CB1_{Bi_2Se_3}$ states well below E_F around Γ but above E_F everywhere else in the BZ. The overall picture is that charge transfer from the Bi_2 layer to the Bi_2Se_3 layer drives the system, theoretically, to a weak topological semimetal, and including hybridization and bonding between the layers drives the system into the observed strong topological semimetal. Therefore, both ionic and covalent interactions between the layers play a key role in the topology of the electronic structure.

The combination of the Bi_2Se_3- and Bi_2-based surface states, along with the bulk bands crossing the Fermi level, make for a relatively complicated measured Fermi surface. However, comparison between the symmetrized ARPES data and DFT calculations gives insight to the electronic structure around the Fermi energy, and allows for the construction of schematic constant energy contours (CECs) [Figs. 4(c) and 4(f)] and the identification of observed bands. The bands are identified

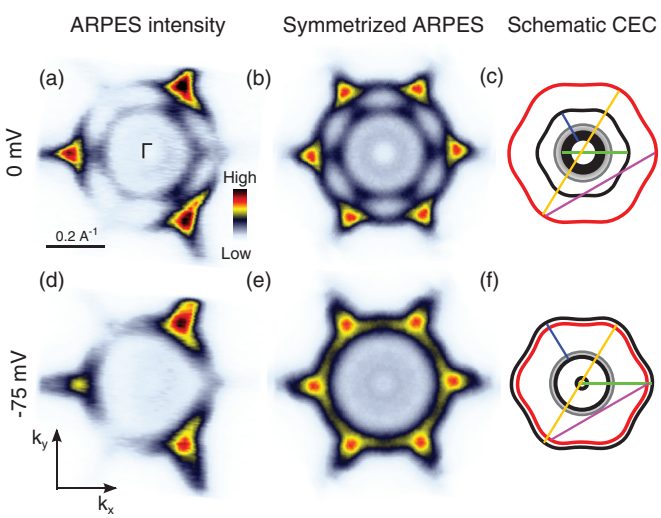

FIG. 4. (Color online) (a), (d) The ARPES intensity slices corresponding to the Fermi surface ($E = 0$ meV) and $E = -75$ meV, respectively. Directions $\bar{\Gamma} - \bar{M}$ and $\bar{\Gamma} - \bar{K}$ are along k_x and k_y, respectively. (b), (e) Symmetrized ARPES data for $E = 0$ and -75 meV. (c), (f) Schematic constant energy contours (CEC)s constructed from comparing the ARPES data with the calculations, for the Bi_2 termination, presented on the same scale as the symmetrized ARPES data. Red, black, and gray lines are from the Bi_2Se_3 surface states, Bi_2 surface states, and bulk bands, respectively. Blue and green lines mark the dominant scattering vectors observed in STM. The orange and violet lines mark possible scattering vectors which are present in JDOS but not seen in STM data (see Fig. 5).

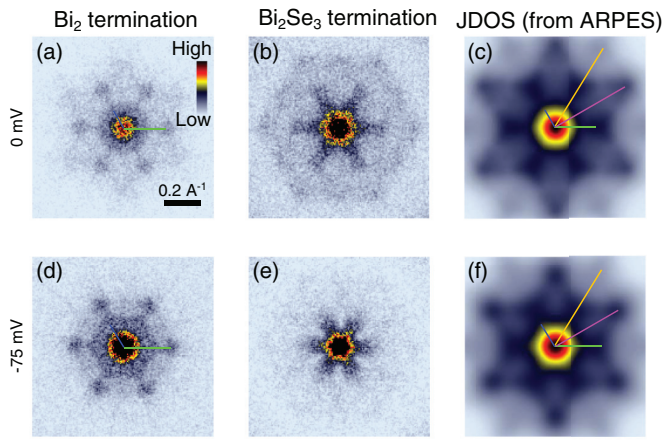

FIG. 5. (Color online) (a), (d) Fourier transform of the STM conductance map on the Bi_2-terminated surface for $V = 0$ and -75 mV. The color map shows intensities from white-blue (low) to red-black (high). The scattering vectors corresponding to the inner surface structure of the Bi bilayer to the outer bands along the $\bar{\Gamma} - \bar{M}$ direction is marked by the blue and green lines (compare to Fig. 4). (b), (e) Fourier transform of the STM conductance for the same voltages on the Bi_2Se_3 surface. (c), (f) Joint density of states calculated using ARPES data corresponding to the Fermi surface and $E = -75$ meV. The blue, green, orange, and violet lines mark the possible scattering vectors (blue and green are seen in STM data, compare also to Fig. 4).

as either Bi_2-derived surface states (black), Bi_2Se_3-derived surface states (red), or bulk states. We note that while the second highest k state at E_F and the highest k state at -75 meV have been identified as a Bi_2-derived surface state (the outermost black lines in the CECs), this state crosses the Fermi energy an even number of times and does not span any continuous gap; it is therefore most likely a trivial surface state. The other states identified as Bi_2- or Bi_2Se_3-derived surface states are the TSS discussed earlier.

To investigate the local spectroscopic signatures of the two surfaces and make a connection to the ARPES data, we performed STM of the interference patterns caused by surface defects (Fig. 5). In the range of -100 to $+100$ mV, we observe QPI patterns on both Bi_2- and Bi_2Se_3-terminated surfaces. The Fourier transform of the real-space conductance map can be linked directly to the joint density of states (JDOS) calculated using ARPES data [see Figs. 5(c) and 5(f)]. Importantly, on both surfaces we observe an overall suppression of the scattering intensity. The observed suppression is at least partly due to backscattering protection coming from the spin texture, as in the case of usual topological insulator surfaces.[27] This is consistent with previous spin-resolved ARPES experiments on $Bi_4Se_{2.4}S_{0.6}$.[25] The only well-resolved scattering vectors are the ones along the $\bar{\Gamma}$-$\bar{M}$ direction, marked by blue and green lines in Fig. 5(a). These vectors can be easily identified as the scattering from the inner ringlike parts of the Bi_2 surface bands close to the outer bands which are not protected by spin texture [see also Fig. 4(c)]. Note that in vicinity of the outer ring there is also a bulk band [marked gray line in Figs. 4(c) and 4(f)]. Although this band somewhat complicates the exact interpretation, it is reasonable to expect that scattering from the surface state

dominates the STM signal. However, in order to make exact quantitative comparison between STM data and JDOS details of the hybridization between bulk and surface bands have to be taken into account. This may be the subject of future study.

In conclusion, we have shown that TSS are observed on both types of cleaved surfaces of the natural superlattice phase Bi_4Se_3. The dispersion and Kramers point energy of the TSS are shown to differ between the two surface terminations, and from simple expectations. This provides an example of distinct TSS on different surfaces with the same crystallographic orientation in a complex material. Finally, we show that the bulk topological index is due to a combination of ionic and covalent interactions between the building blocks, and that the difference in the TSS in Bi_4Se_3 is likely due to the different properties of the two layer types. This suggests that modification of the TSS on the surfaces of topological materials may be experimentally realizable in the large family of natural superlattice materials in the Bi_2-Bi_2Se_3, Bi_2-Bi_2Te_3, and Sb_2-Sb_2Te_3 systems, and hints at a complex topological phase diagram in these superlattice families.

The authors acknowledge helpful discussions with B. A. Bernevig and F. Chen. The financial support of the National Science foundation, Grants No. NSF-DMR-0819860 and No. NSF-DMR-1104612, DARPA-SPAWAR Grant No. N6601-11-1-4110, and the ARO MURI program, Grant No. W911NF-12-1-0461, are gratefully acknowledged. The work at Brookhaven was carried out in part at the Center for Functional Nanomaterials and the National Synchrotron Light Source which are supported by the US Department of Energy (DOE), Office of Basic Energy Sciences, under Contract No. DE-AC02-98CH10886. The Advanced Light Source is supported by the US DOE, Office of Basic Energy Sciences, under Contract No. DE-AC02-05CH11231. One of the authors (S.N.-P.) acknowledges support of European Community through the Marie-Curie OEF fellowship.

*rcava@princeton.edu

[1] L. Fu, C. L. Kane, and E. J. Mele, Phys. Rev. Lett. **98**, 106803 (2007).
[2] H. Lin, R. S. Markiewicz, L. A. Wray, L. Fu, M. Z. Hasan, and A. Bansil, Phys. Rev. Lett. **105**, 036404 (2010).
[3] M. Neupane, S. Xu, L. Wray, A. Petersen, R. Shankar, N. Alidoust, C. Liu, A. Fedorov, H. Ji, J. Allred *et al.*, Phys. Rev. B **85**, 235406 (2012).
[4] D. Hsieh, D. Qian, L. Wray, Y. Xia, Y. Hor, R. Cava, and M. Hasan, Nature (London) **452**, 970 (2008).
[5] H.-J. Noh, H. Koh, S.-J. Oh, J.-H. Park, H.-D. Kim, J. Rameau, T. Valla, T. Kidd, P. Johnson, Y. Hu *et al.*, Europhys. Lett. **81**, 57006 (2008).
[6] D. Hsieh, Y. Xia, D. Qian, L. Wray, J. Dil, F. Meier, J. Osterwalder, L. Patthey, J. Checkelsky, N. Ong *et al.*, Nature (London) **460**, 1101 (2009).
[7] D. Hsieh, Y. Xia, D. Qian, L. Wray, F. Meier, J. Dil, J. Osterwalder, L. Patthey, A. Fedorov, H. Lin *et al.*, Phys. Rev. Lett. **103**, 146401 (2009).
[8] Y. L. Chen, J. G. Analytis, J.-H. Chu, Z. K. Liu, S.-K. Mo, X. L. Qi, H. J. Zhang, D. H. Lu, X. Dai, Z. Fang, S. C. Zhang, I. R. Fisher, Z. Hussain, and Z.-X. Shen, Science **325**, 178 (2009).
[9] Y. L. Chen, Z. K. Liu, J. G. Analytis, J.-H. Chu, H. J. Zhang, B. H. Yan, S.-K. Mo, R. G. Moore, D. H. Lu, I. R. Fisher, S. C. Zhang, Z. Hussain, and Z.-X. Shen, Phys. Rev. Lett. **105**, 266401 (2010).
[10] H. Zhang, C.-X. Liu, X.-L. Qi, X. Dai, Z. Fang, and S.-C. Zhang, Nat. Phys. **5**, 438 (2009).
[11] T. Sato, K. Segawa, H. Guo, K. Sugawara, S. Souma, T. Takahashi, and Y. Ando, Phys. Rev. Lett. **105**, 136802 (2010).
[12] Z. Ren, A. A. Taskin, S. Sasaki, K. Segawa, and Y. Ando, Phys. Rev. B **82**, 241306 (2010).
[13] R. Takahashi and S. Murakami, Phys. Rev. Lett. **107**, 166805 (2011).
[14] A. A. Burkov and L. Balents, Phys. Rev. Lett. **107**, 127205 (2011).
[15] H. Jin, J. Im, J.-H. Song, and A. J. Freeman, Phys. Rev. B **85**, 045307 (2012).
[16] L. Miao, Z. F. Wang, W. Ming, M.-Y. Yao, M. Wang, F. Yang, Y. R. Song, F. Zhu, A. V. Fedorov, Z. Sun, C. L. Gao, C. Liu, Q.-K. Xue, C.-X. Liu, F. Liu, D. Qian, and J.-F. Jia, Proc. Natl. Acad. Sci. USA **110**, 2758 (2013).
[17] T. Hirahara, G. Bihlmayer, Y. Sakamoto, M. Yamada, H. Miyazaki, S.-i. Kimura, S. Blügel, and S. Hasegawa, Phys. Rev. Lett. **107**, 166801 (2011).
[18] X. He, W. Zhou, Z. Y. Wang, Y. N. Zhang, J. Shi, R. Q. Wu, and J. A. Yarmoff, Phys. Rev. Lett. **110**, 156101 (2013).
[19] H. Lin, T. Das, Y. Okada, M. C. Boyer, W. D. Wise, M. Tomasik, B. Zhen, E. W. Hudson, W. Zhou, V. Madhavan, C.-Y. Ren, H. Ikuta, and A. Bansil, Nano Lett. **13**, 1915 (2013).
[20] P. Bayliss, Am. Mineral **76**, 257 (1991).
[21] S. Murakami, Phys. Rev. Lett. **97**, 236805 (2006).
[22] J. W. G. Bos, H. W. Zandbergen, M.-H. Lee, N. P. Ong, and R. J. Cava, Phys. Rev. B **75**, 195203 (2007).
[23] P. Blaha, K. Schwarz, P. Sorantin, and S. Trickey, Comput. Phys. Commun. **59**, 399 (1990).
[24] J. P. Perdew, K. Burke, and M. Ernzerhof, Phys. Rev. Lett. **77**, 3865 (1996).
[25] T. Valla, H. Ji, L. Schoop, A. Weber, Z. Pan, J. Sadowski, E. Vescovo, A. Fedorov, A. Caruso, Q. Gibson *et al.*, Phys. Rev. B **86**, 241101 (2012).
[26] D. Hsieh, Y. Xia, L. Wray, D. Qian, A. Pal, J. Dil, J. Osterwalder, F. Meier, G. Bihlmayer, C. Kane *et al.*, Science **323**, 919 (2009).
[27] P. Roushan, J. Seo, C. V. Parker, Y. S. Hor, D. Hsieh, D. Qian, A. Richardella, M. Z. Hasan, R. J. Cava, and A. Yazdani, Nature (London) **460**, 1106 (2009).